Ocean Engineering 77 (2014) 23–32

Contents lists available at ScienceDirect

Ocean Engineering

journal homepage: www.elsevier.com/locate/oceaneng

Reduction of propeller cavitation induced hull exciting pressure by a reflected wave from air-bubble layer

Jeung-Hoon Lee *, Hyoung-Gil Park **, Jin-Hak Kim, Kyung-Jun Lee, Jong-Soo Seo

Samsung Ship Model Basin (SSMB), Marine Research Institute, Samsung Heavy Industries, Science Town, Daejeon 305-380, South Korea

ARTICLE INFO

Article history:
Received 20 April 2013
Accepted 14 December 2013
Available online 3 January 2014

Keywords:
Propeller
Cavitation
Air-bubble layer
Reflection

ABSTRACT

Cavitation generated by marine propellers is one of the main sources of vibration and noise in commercial ships. By taking advantage of the compressibility of air, there have been many attempts to form an air-bubble layer underneath the stern-hull surface above the propeller, and consequently to isolate the cavity induced pressure wave across the layer. However, this approach is not widely used because the cost to deliver a sufficiently large amount of air for isolation is prohibitive. In this study, full-scale ship measurements proved that the pressure amplitude can be significantly reduced outside an air-bubble layer where the isolation effect has not been applied. A hull-vibration reduction of approximately 75% was achieved. Only a small amount of air is needed to reduce the cavitation-induced pressure amplitude, so the system to produce the air layer becomes simple. The purpose of this study was to provide physical evidence that this phenomenon was achieved. The solution of acoustic scattering from a bubble was approximated to show that the main reason for the reduced pressure outside the layer is phase reversal reflection, which provokes destructive interference.

© 2013 Elsevier Ltd. All rights reserved.

1. Introduction

Cavitation is the process of nucleation in a liquid when the pressure falls below the vapor pressure (Brennen, 1995). After the pressure again increases to above the critical value, the vapor bubbles that formed around the nuclei begin to implode before finally disappearing. The violent cavity collapse takes place very quickly over several microseconds while radiating pressure waves into the surrounding liquid. The most serious occurrences are caused by marine propellers (Ross, 1976).

As the propeller blades rotate behind the ship, each blade experiences fluctuations in inflow velocity and hydrostatic pressure, resulting in periodic occurrences of cavitation (Carlton, 2007). The pressure fluctuation caused by cavitation exerts a vibratory excitation force on the hull surface above the propeller. These forces can be several hundred kilo-Newtons at multiples of the blade passage frequency (BPF). Thus, propeller cavitation together with the main engine is considered the primary source of vibration and noise on a ship (Nilsson, 1980; Weitendorf, 1981). In order to prevent or control such harmful effects while maintaining the propulsion efficiency at the desired level, ship designers have devoted considerable efforts to diminish excitation forces below certain limits in order to prevent severe vibration and noise problems or meet contract specifications.

Although designs have been substantially improved with the development of the highly skewed propeller (Cumming et al., 1972), further mitigation of the propeller excitation force depends on external devices that affect the inflow: for example, a flow control duct (Lindgren and Johnsson, 1980) or fin (Friesch, 1992). Soon after these innovations, the air-bubble layer was introduced to marine vessels: compressed air is continuously injected by a system of nozzles located on the hull in front of the propeller to form an air-bubble layer underneath the stern of the hull surface. The large number of air bubbles in the layer can be approximated as a single macrobubble (Carstensen and Foldy, 1947). The stiffness characteristic of air (Lee and Kim, 2007, 2009) and the small mass of seawater adjacent to the bubble then constitute an isolation system whose resonance frequency is inversely proportional to the equivalent bubble size (Minnaert, 1933). Thus, a cavitation-induced pressure wave should be isolated across the layer above the resonance frequency.

Based on model-scale measurements in a water cavitation tunnel, Ukon et al. (2000) demonstrated the benefits of an air-bubble layer for pressure excitation reduction. The tests were conducted without air injection and with air injection at different flow rates. At small amounts of air injection, i.e., when the resonance frequency of the air bubbles was not sufficiently low, the pressure amplitude at the first BPF increased greatly compared to that of the no-injection case. However, further increasing the

* First author. Tel.: +82 42 865 4378; fax: +82 42 865 4380.
** Corresponding author. Tel.: +82 42 865 4372; fax: +82 42 865 4380.
E-mail addresses: jhope.lee@samsung.com (J.-H. Lee), h-gil.park@samsung.com (H.-G. Park).

0029-8018/$ - see front matter © 2013 Elsevier Ltd. All rights reserved.
http://dx.doi.org/10.1016/j.oceaneng.2013.12.007

Nomenclature

a	radius of spherical bubble [m]
B	bulk modulus of air under an adiabatic condition, [N/m^2]
c	speed of sound [m/s]
f	frequency [Hz]
ϕ	azimuth angle [rad]
g	relative density, ρ_b/ρ_w
γ (=1.4)	specific heat ratio of air
h	relative acoustic speed, c_b/c_w
Im	imaginary part of complex variable
i	$\sqrt{-1}$
j_m	mth order spherical Bessel function
k	wavenumber [rad/m]
m	order of the scattered wave
n_m	mth order spherical Neumann function
P	pressure, [Pa]
p_{inc}	incident plane wave pressure [Pa]
p_0	amplitude of incident plane wave [Pa]
p_{scat}	scattered wave pressure [Pa]
p_{total}	total pressure ($=p_{inc}+p_{scat}$) [Pa]
P_m	mth order Legendre function
Q	airflow rate [m^3/s]
θ	polar angle [rad]
Re	real part of complex variable
r	radial distance from the origin of spherical bubble [m]
ρ	density [kg/m^3]
t	time [s]
V	volume, [m^3]
ω	frequency [rad/s]

Subscripts

0	equilibrium
b	air-bubble
res	resonance
w	seawater

injection to lower the resonance frequency showed the extent of the isolation effect. Full-scale application of the air-bubble layer was examined by Krüger et al. (2004) and Ødegaard (2006), who found that the isolation performance was mainly effective at high frequencies. Inadequate injection owing to limited air compressor capacity seems to have caused the failure at low frequencies around the first BPF.

Because the previous studies simply exploited the isolation effect of air bubbles, they had to distribute the air bubbles around the whole wetted hull surface, as shown in Fig. 1(a). Hence, the spatial arrangement of several nozzles and relevant complex piping systems was indispensable; this can be hindered by the shipbuilding environment or maintenance issues. Furthermore, the huge air-compressor capacity required to supply plenty of air is a critical bottleneck because it requires considerable power consumption. Thus, air-bubble layers have not come into widespread use for conventional designs.

Our current efforts followed the approach of previous studies and were expected to realize the same effect. As shown in Fig. 1(b), a single-nozzle arrangement that distributes air bubbles around the maximum pressure amplitude only was attempted to save energy. When the airflow rate was varied, measurements at the interior of the air-bubble layer clearly showed similar behavior as in previous studies. A significant reduction in the pressure amplitude (especially for the first BPF) was also observed at the exterior of the air layer, where the isolation effect of air bubbles was not expected. As a result, hull vibrations at the corresponding frequency were reduced by approximately 75%. This implies that the conventional air-injection system can be simplified to an efficient design that reduces excessive air consumption and simplifies complex piping works. In order to explain the unforeseen benefit, we were inspired by the scattering (or reflection) from the pressure release boundary of a water-to-air interface (Kim, 2010), whereupon destructive interference occurs around the bubble. By employing acoustical scattering from a bubble (Anderson, 1950) followed by low-frequency approximation, we present a qualitative description of measurements at both the exterior and interior of the layer.

Section 2 presents the air-injection test on a full-scale ship, which was our motivation for this study. Section 3 covers the development of a theoretical formulation and its comparison with the measured data. Finally, this paper closes with conclusions in Section 4.

2. Air-injection test on full-scale ship

2.1. Experimental setup

Table 1 summarizes the specifications of the test vessel, which was built by Samsung Heavy Industries in 2012. The ship is a commercial 8000 TEU container vessel with a nine-cylinder two-stroke diesel engine and six-bladed propeller. Fig. 2 shows the schematic; the air-injection system comprises an air compressor (power rating: 35 kW), piping, and a nozzle, and it was installed on the aft of the ship. Fig. 3 shows the nozzle plugged into the hull surface through the four penetrations. A flow regulator was fitted into the pipeline to control and read the airflow rate. As shown in Fig. 4, three pressure sensors (Model: Kulite XTL-190) were flush-mounted to the hull at 2 m intervals on the propeller plane.

To specify the location of the nozzle, propeller cavitation tests were previously conducted with a model-scale ship at the water tunnel in the Samsung Ship Model Basin (SSMB) to measure the distribution of pressure fluctuations over the stern of the hull. Based on the model-test results and considering shipbuilding allowances, the nozzle was positioned 4 m directly ahead of P1 so that the injected air bubbles could cover the area of maximum pressure amplitude. An underwater viewing borescope (Model: Olympus R100-025) shown in Fig. 5 was installed at the centerline of the hull and 2 m ahead of P2 to observe how the air bubbles developed around the stern of the hull surface. Finally, the two accelerometers (Model: PCB 352C66) shown in Fig. 2 were attached to the transom and accommodation structure to evaluate the reduction in vibration with air injection.

When the rotational speed of the propeller was maintained at 100 rpm (1.67 Hz), the ship speed was 22.1 kn when going in a straight line at a Beaufort scale of 2 (Wikipedia, 2013). The tests were conducted without air injection and with air injection at four different airflow rates: $Q_1=2.4$ m^3/min, $Q_2=3.1$ m^3/min, $Q_3=3.8$ m^3/min, and $Q_4=4.5$ m^3/min. The signals from the pressure sensors and accelerometers were passed through a signal conditioner and logged into a computer-based dynamic signal analyzer (B&K Pulse system) with a sampling frequency of 256 Hz. A fast Fourier transform was then used to obtain the amplitude spectrum in the frequency domain. The spectrum was estimated by applying the Hanning window and finding the ensemble average of 20 times with 75% overlapping; it was observed at a frequency resolution of 0.125 Hz (Bendat and Piersol, 2010).

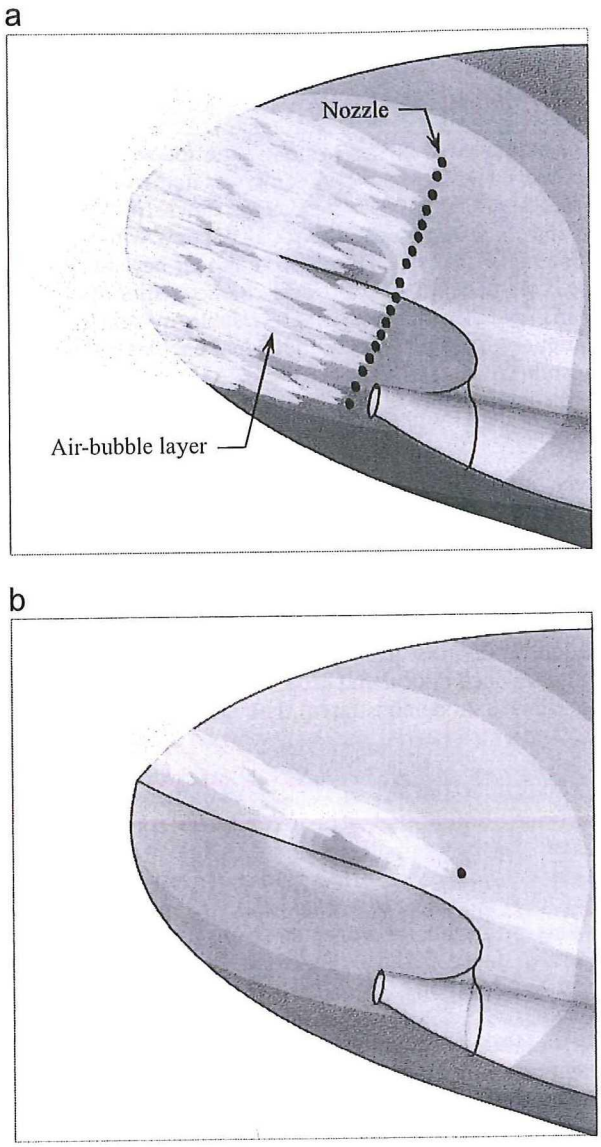

Fig. 1. Conceptual sketch for air-bubble layer (propeller is not shown). The contour coloring on the hull surface represents an example distribution of the pressure amplitude at the first BPF: (a) spatial arrangement of several nozzles, (b) single-nozzle arrangement. (For interpretation of the references to color in this figure legend, the reader is referred to the web version of this article).

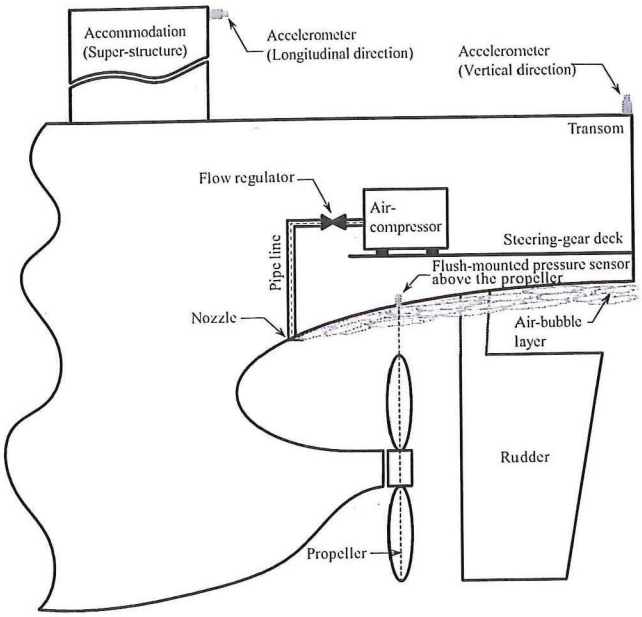

Fig. 2. Arrangement of air-injection system in aft of ship.

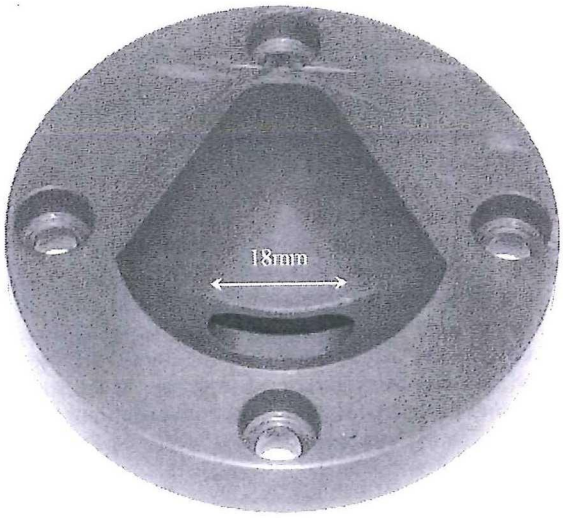

Fig. 3. Detail picture of nozzle. The protruded outlet aligned parallel to the hull surface has a nearly circular shape with an equivalent diameter of approximately 18 mm. Compared to the size of the mooring lug shown in Fig. 6(c), the nozzle is not considered to affect the hull resistance.

Table 1
Specifications of test vessel: 8000 TEU Container vessel.

Item	Value
Length between perpendicular, [m]	285
Breadth, [m]	45.6
Draught, [m]	12.5
Maximum main engine power [kW]	43,608
Propeller diameter, [m]	8.6
Number of propeller blades	6
Propeller RPM during test	100
Ship speed during test, [knots]	22.1

2.2. Results

Fig. 6 represents the images captured at the maximum airflow rate Q_4. As soon as the air departed the nozzle, it violently began to spread as it moved downstream and eventually formed a triangular layer with a finite thickness. The air-bubble coverage on the maximum pressure area near P1 was confirmed, as shown in Fig. 6(c). When the layer was approximated as a thin wedge, its cross-sectional area at the propeller plane can be roughly estimated by the size of the mooring lug, which is shown in the accompanying image. The dimensions for each air low rate are listed in Table 2, which we return to in Section 3.

Fig. 7 shows the amplitudes of the pressure fluctuation and acceleration at several multiples of the blade rates. All of the values were normalized against the data without injection to investigate relative changes after injection. The pressure amplitude was found to largely depend on whether or not the measurement took place inside the layer.

At P1, where the hull was covered by air bubbles, the responses were quite similar to the results of previous works (Ukon et al., 2000; Krüger et al., 2004; Ødegaard, 2006). At low air injection flow rates (Q_1 and Q_2), the amplification of the pressure amplitude

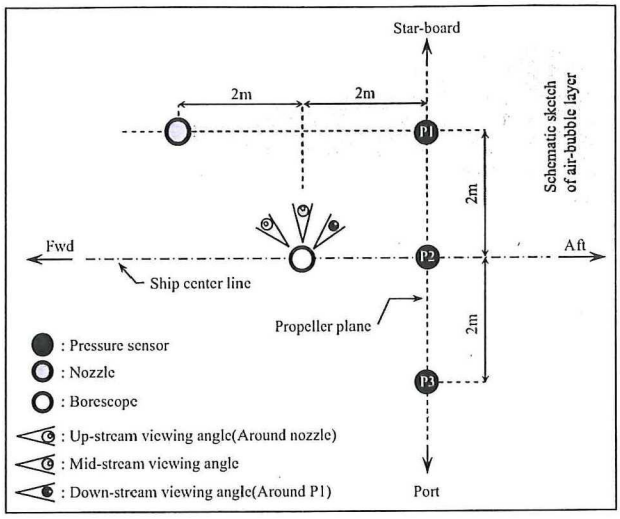

Fig. 4. Locations of pressure sensors, nozzle, and borescope on hull stern (top view). Three different viewing angles from the borescope are also depicted.

at the first BPF can be justified by the resonance of the air bubbles. High-order components were reduced by the isolation effect beyond the resonance. Increasing the airflow rate corresponded to an increase in the equivalent bubble size for the bubble cloud, which lowered the resonance frequency. Hence, higher air injection flow rates (Q_3 and Q_4) moderated the first BPF components and isolated high-order ones.

The measurements outside layer P2 and P3 demonstrated somewhat interesting behavior. When the air injection was small (Q_1 and Q_2), the bubble resonance seemed to have a first-order effect on the amplification. Despite this, the high-order values depicted unexpected reductions; they degraded with frequency and distance from the air layer. Considering the measurement uncertainties,[1] the high-frequency amplitudes still tended to gradually decrease with increased injection. More surprisingly, the first-order pressure amplitudes for high injection cases (Q_3 and Q_4) were suddenly reduced by a significant degree; thus, vibrations at the corresponding frequency also diminished. Particularly for the airflow rate Q_4, vibration was reduced at the first BPF by about 75%. This performance is satisfactory since the first-order BPF is vitally important to controlling ship vibrations. Although we did not achieve similarly remarkable reductions for higher harmonic vibrations, the reductions were 10–20%.

The experimental results in this study provide evidence of the reduced pressure amplitude outside the layer. In acoustic theory, an acoustic wave that meets a boundary with a different characteristic impedance is partly transmitted and partly reflected. A pressure release boundary formed by a plane interface between water and air reflects incident waves in an out-of-phase manner (Kim, 2010). When the reflected wave is superposed on the incident, the amplitude of the resulting total wave becomes zero. This is called destructive interference, which was anticipated to hold for a non-planar boundary case, i.e., the air bubbles. As discussed in the next section, we continued to explore this acoustic feature.

[1] In normal practice, the signal-to-noise ratio becomes weak with the frequency. This was also the case in our measurement, as shown by comparing the error bars in Fig. 7 for the high- and low-order components. Hence, the relative representation for high-order components may exaggerate such measurement uncertainties.

3. Theoretical pressure reduction outside air-bubble layer

3.1. Solution of acoustic scattering from bubble and its low-frequency approximation

For simplified analysis, we made the following assumptions. As shown in Fig. 6, the air layer comprises numerous individual air bubbles. These air bubbles are flowing downstream with continuous injection. Analyzing individual bubbles with their motion and interaction is extremely difficult and far beyond our research scope. Traditionally, the acoustical characteristics of bubble flow are analyzed according to single bubble dynamics under the assumption that the effects of individual bubbles can be algebraically summed. Carstensen and Foldy (1947) introduced the effective medium theory that regards a bubble cloud as a single scattered object with uniform acoustic properties. Although the theory loses validity when the bubble concentration becomes greater, it has been experimentally verified at low frequencies (Nicholas et al., 1994). This encourages the assumption of the bubble cloud as an equivalent spherical bubble (filled with pure air) keeping a stationary position in space. However, the equivalent bubble assumption can be off without appropriate validation based on estimations of the void fraction and bubble size distribution. Several researchers (Johansen et al., 2010; Terril and Fu, 2008) developed optical and acoustical methods to measure two-phase flow and demonstrated their applicability on full-scale ships. Unfortunately, in our case, we had almost no chance to attempt such methodologies in a full-scale environment due to instrumentation limitations. Thus, we adhered to the above assumption without validation in order to produce a practical solution.

Next, the incident wave representing a pressure fluctuation from a cavitating propeller was assumed to be planar. The acoustic modeling for cavitation is often handled by a number of monopoles or, perhaps more accurately, by additional dipoles (Wijngaarden et al., 2006; Kinns and Bloor, 2004). However, the wavelengths for the blade rates under consideration were large compared to the size of the equivalent bubble. Thus, the plane wave assumption for the incident case is reasonable.

Finally, reflection by the hull-plate was not considered. At low frequencies, the hull-plate can be regarded as a rigid wall from which reflection results in doubled pressure (Kim, 2010) around the seawater interface with the hull. Thus, the pressure amplitude would be uniformly amplified for the low frequency range of interest. However, the purpose of this study was to explain the experimental results qualitatively, not quantitatively. Therefore, the presence of the hull and the accompanying reflection was considered to be negligible.

Based on the above three assumptions, the scattering problem for a spherical bubble can be defined as shown in Fig. 8; the solution was published by Anderson (1950). His formulations are as follows. An air bubble sphere of radius a whose acoustical impedance is characterized by multiplying ρ_b ($=1.02$ kg/m^3) and c_b ($=340$ m/s) is located at the origin of a spherical coordinate system with the radial distance r, polar angle ϕ, and azimuth angle θ or a Cartesian coordinate system with x–z. ρ_w ($=1024$ kg/m^3) and c_w ($=1500$ m/s) denote the density and speed of sound, respectively, for the surrounding medium, which is seawater. Further, k_b ($=\omega/c_b$) and k_w ($=\omega/c_w$) are the wavenumbers of the air bubble and seawater, respectively, where ω ($=2\pi f$) is the angular frequency in radians per second.

The incident plane wave $p_{inc}=p_0e^{-ik_wz}$travels in the negative z direction and impinges upon the sphere to produce the internal wave p_{int} and external scattered wave p_{scat}. The time factor $e^{-i\omega t}$ is suppressed for compactness. When the bubble is absent, scattering obviously does not take place. Thus, the magnitude of the

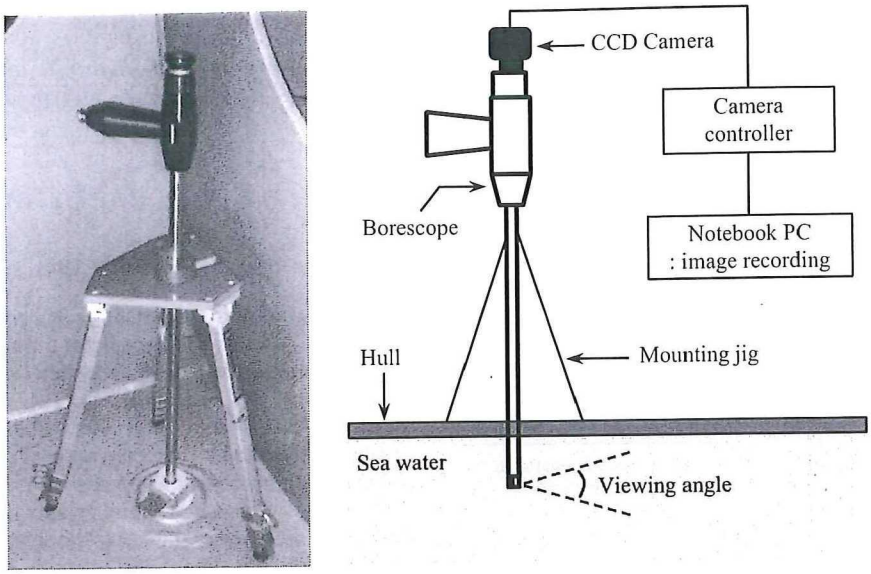

Fig. 5. Borescopic camera system (Model: Olympus R100-025) for underwater viewing.

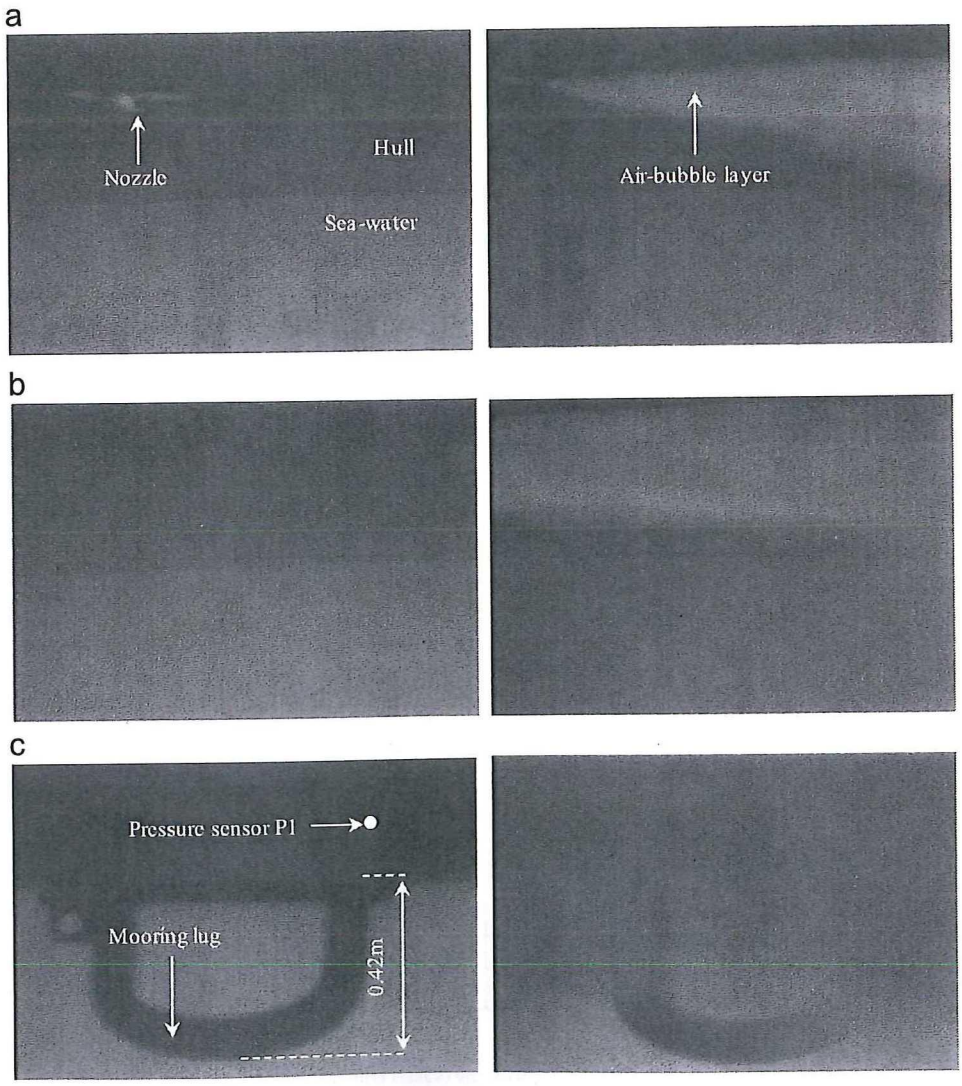

Fig. 6. Examples of underwater viewing images (viewing angles are defined in Fig. 4). Left column: no air injection; right column: air injection with airflow rate Q_4. (a) Upstream view (around nozzle), (b) midstream view, (c) downstream view (around pressure sensor P1).

incident pressure p_0 is actually the pressure amplitude without air injection. The total pressure outside the bubble, which is measured by a transducer, is the summation of p_{inc} and p_{scat}. By employing spherical harmonics (Morse and Ingard, 1987) to represent these waves, Anderson successfully derived the solution to the scattered pressure p_{scat} as a series of modal terms:

$$p_{scat}(r,\theta) = -p_0 \sum_{m=0}^{\infty} \left[(-i)^m \frac{(2m+1)}{1+iC_m} \right] P_m(\cos\theta)[j_m(k_w r) + i n_m(k_w r)] \tag{1}$$

The dependence of p_{scat} on the polar angle ϕ can be eliminated by choosing the incident plane wave parallel to the polar axis.

Table 2
Rough dimensions of air-bubble layer at propeller plane.

Airflow rate, [m³/min]	Width of layer, w [m]	Thickness of layer, t [m]	Cross-sectional area, $w \times t$ [m²]
Q_1 (2.4)	1.70	0.10	0.17
Q_2 (3.1)	1.80	0.15	0.27
Q_3 (3.8)	1.90	0.20	0.38
Q_4 (4.5)	2.00	0.25	0.50

C_m in Eq. (1) is given as follows:

$$C_m = \frac{[\alpha_m(k_b a)/\alpha_m(k_w a)][n_m(k_w a)/j_m(k_a a)] - [\beta_m(k_w a)/\alpha_m(k_w a)]gh}{[\alpha_m(k_b a)/\alpha_m(k_w a)][j_m(k_w a)/j_m(k_a a)] - gh} \tag{2}$$

$$\alpha_m(k_{b,w}a) = m j_{m-1}(k_{b,w}a) - (m+1) j_{m+1}(k_{b,w}a) \tag{3}$$

$$\beta_m(k_{b,w}a) = m n_{m-1}(k_{b,w}a) - (m+1) n_{m+1}(k_{b,w}a), \tag{4}$$

where g is the relative density ρ_b/ρ_w and h is the relative acoustic speed c_b/c_w. Also, m is the order of the scattered wave, P_m the m-th order Legendre function, j_m the spherical Bessel function, and n_m the spherical Neumann function.

However, the series solution in Eq. (1) is not appropriate to qualitatively explain the behavior of scattered waves. We used the following approximations for the series. At low frequencies where the product of the wavenumber and radius of sphere a is much less than unity, i.e., $k_b a$, $k_w a \ll 1$, only the first term in the series needs to be considered. Furthermore, when we are interested in distances several meters away from the macro bubble, a near-field assumption can be employed, i.e., $k_w r \ll 1$.

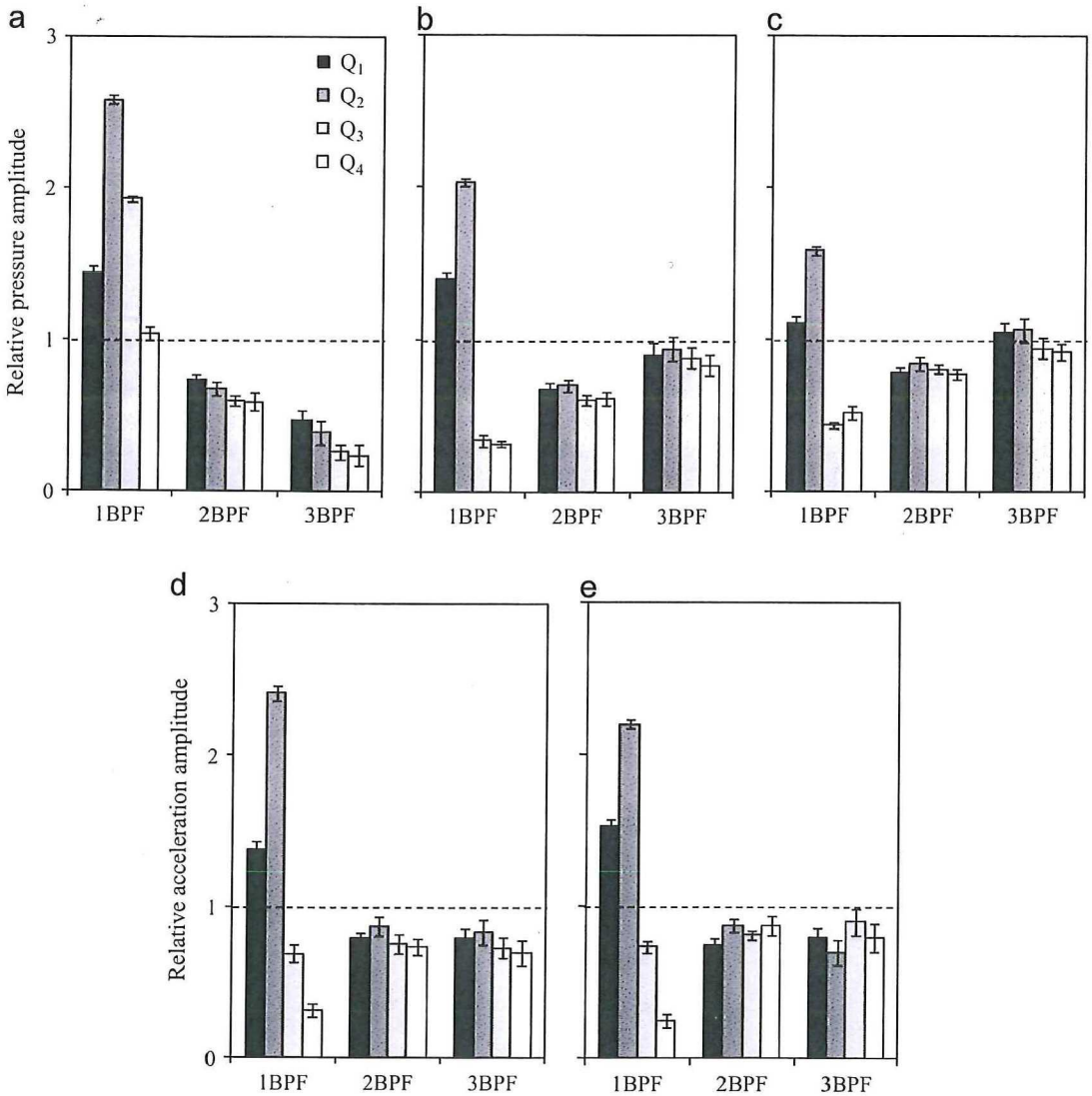

Fig. 7. Measurements of pressure fluctuation and vibration with variation in airflow rate (Values represent relative magnitudes divided by data without injection. The error bars denote a 95% confidence interval.): (a) pressure fluctuation at P1, (b) pressure fluctuation at P2, (c) pressure fluctuation at P3, (d) acceleration at transom, (e) acceleration at accommodation.

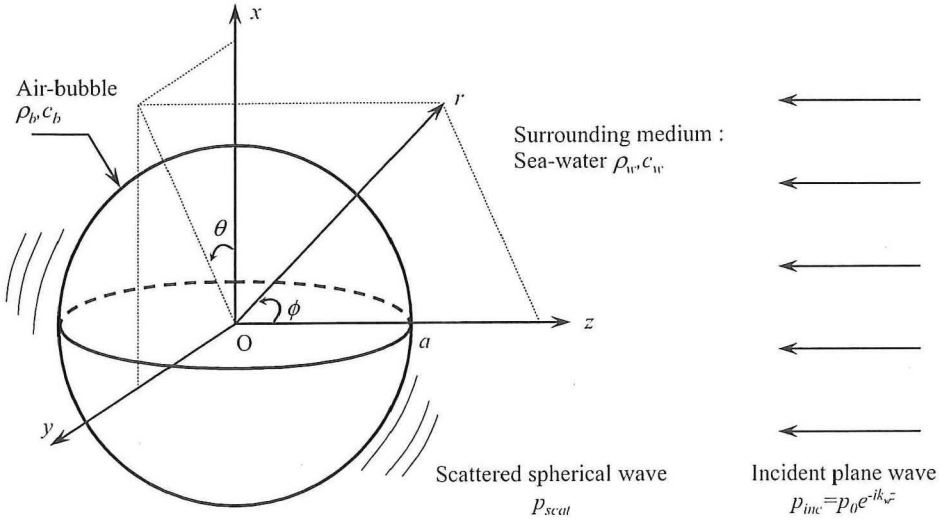

Fig. 8. Model for acoustic scattering from spherical air bubble.

Then, the spherical Bessel and Neumann functions can be approximated as (Morse and Ingard, 1987)

$$j_m(\cdot) \overset{(\cdot)\ll 1}{\Longrightarrow} \frac{(\cdot)^m}{1\times 3\times 5\cdots(2m+1)} \tag{5}$$

$$j_0(\cdot)=1, \quad j_1(\cdot)=(\cdot)/3 \tag{6}$$

$$n_m(\cdot) \overset{(\cdot)\ll 1}{\Longrightarrow} \frac{-1\times 1\times 3\cdots(2m-1)}{(\cdot)^{m+1}} \tag{7}$$

$$n_0(\cdot)=-1/(\cdot), \quad n_1(\cdot)=-1/(\cdot)^2 \tag{8}$$

The lowest-order Legendre function is given by Eq. (9), which eliminates the dependence on θ of p_{scat}

$$P_0(\cos\theta)=1 \tag{9}$$

For the air bubble surrounded by the seawater, gh^2 can be assumed to be much less than the unity. This allows a simpler form of C_0

$$C_0=\frac{3gh^2}{(k_wa)^3(1-gh^2)}-\frac{1}{k_wa(1-gh^2)}\cong\frac{3gh^2}{(k_wa)^3}-\frac{1}{k_wa} \tag{10}$$

When Eqs. (6) and (8)–(10) are substituted into the first term of Eq. (1), the scattered pressure p_{scat} can simply be written as

$$\begin{aligned} p_{scat}(r) &= -p_0\frac{1}{1+iC_0}[j_0(k_wr)+in_0(k_wr)] \\ &= -p_0\frac{(a/r)(k_wa)^2(3gh^2-(k_wa)^2)+i(k_wa)^5(3gh^2/(k_wa)^2-1+a/r)}{(3gh^2-(k_wa)^2)^2} \end{aligned} \tag{11}$$

In the above derivation, the sixth-order terms of k_wa are neglected. Note that p_{scat} subjected to k_ba, k_wa, and $k_wr\ll 1$ depends only on the radial variable r like the omni-directional breathing sphere. Consequently, any points on the bubble boundary ($r=a$) correspond to the measurement location P1, which is at the boundary of the air-bubble layer. In the same way, the measurement locations P2 and P3 can be considered according to their radial distances away from the bubble without considering the angular dependence.

In Fig. 9, the approximated p_{scat} is compared to the series solution of Eq. (1), which was calculated by summing 30 terms. To normalize the representation, the magnitude of the incident pressure p_0 (or pressure amplitude without air injection) was assumed to be unity for the whole frequency range. Provided that k_wa, $k_wr\ll 1$, the simple solution agrees well with the series; thus, our proposed approximation was validated.

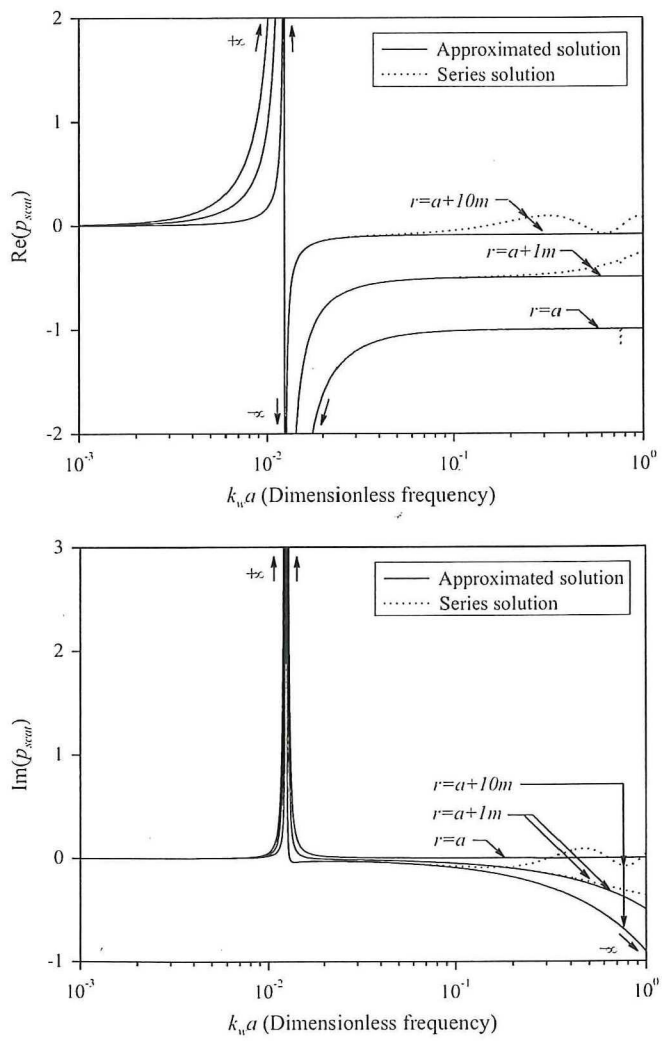

Fig. 9. Comparison of approximated and series solutions for various radial distances r. The amplitude of the incident pressure p_0 was assumed to be unity over the whole frequency range. The radius of the equivalent bubble a was also assumed to be unity.

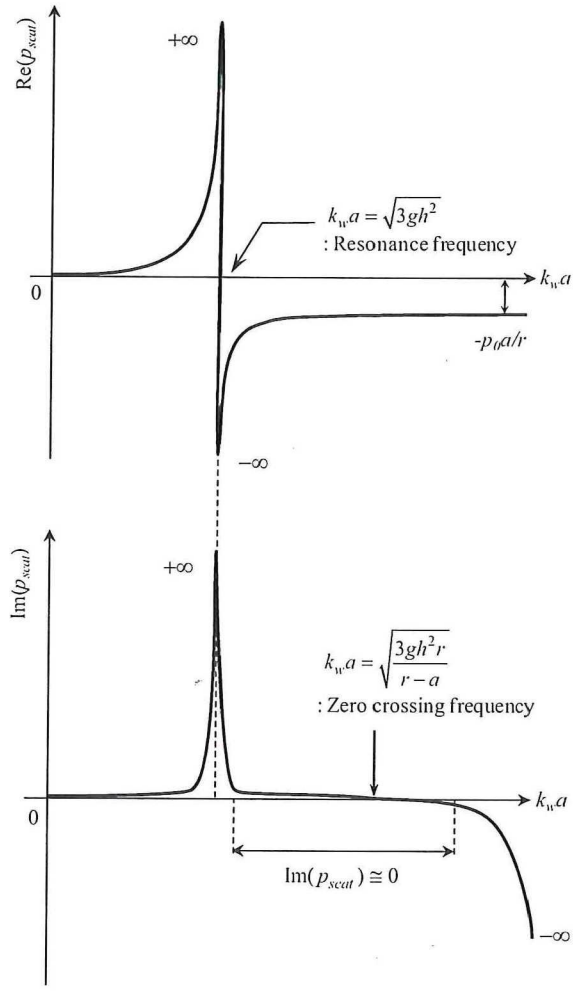

Fig. 10. Schematic sketch for approximated solution of scattered wave p_{scat}.

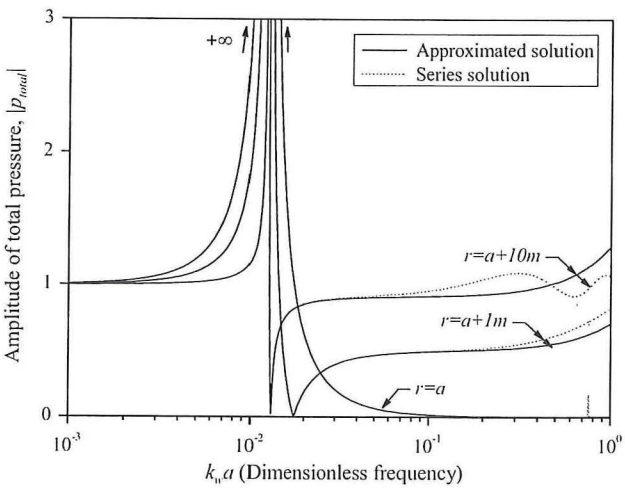

Fig. 11. Amplitude of total pressure $|p_{total}|$. The region where the total pressure is less than the amplitude of the incident pressure p_0, i.e., $|p_{total}| < p_0 = 1$, represents the pressure reduction by destructive interference.

To help understand the behavior of scattered waves, Fig. 10 shows schematics of the approximated p_{scat}. At very low frequencies, both the real (*Re*) and imaginary (*Im*) parts of p_{scat} are nearly zero, which implies that there is no scattering. This becomes apparent with increasing frequency (or $k_w a$); there is then a great

Table 3
List of equivalent bubble radius, resonance frequency, and frequency of maximum destructive interference.

Airflow rate	Equivalent bubble radius, a [m]	Resonance frequency, [Hz]	Frequency of maximum destructive interference, [Hz]		
			$r=a$ (P1)	$r=2$ m (P2)	$r=4$ m (P3)
Q_1	0.23	12.8	∞	13.7	13.2
Q_2	0.30	9.9	∞	10.7	10.3
Q_3	0.35	8.4	∞	9.3	8.9
Q_4	0.40	7.4	∞	8.2	7.8

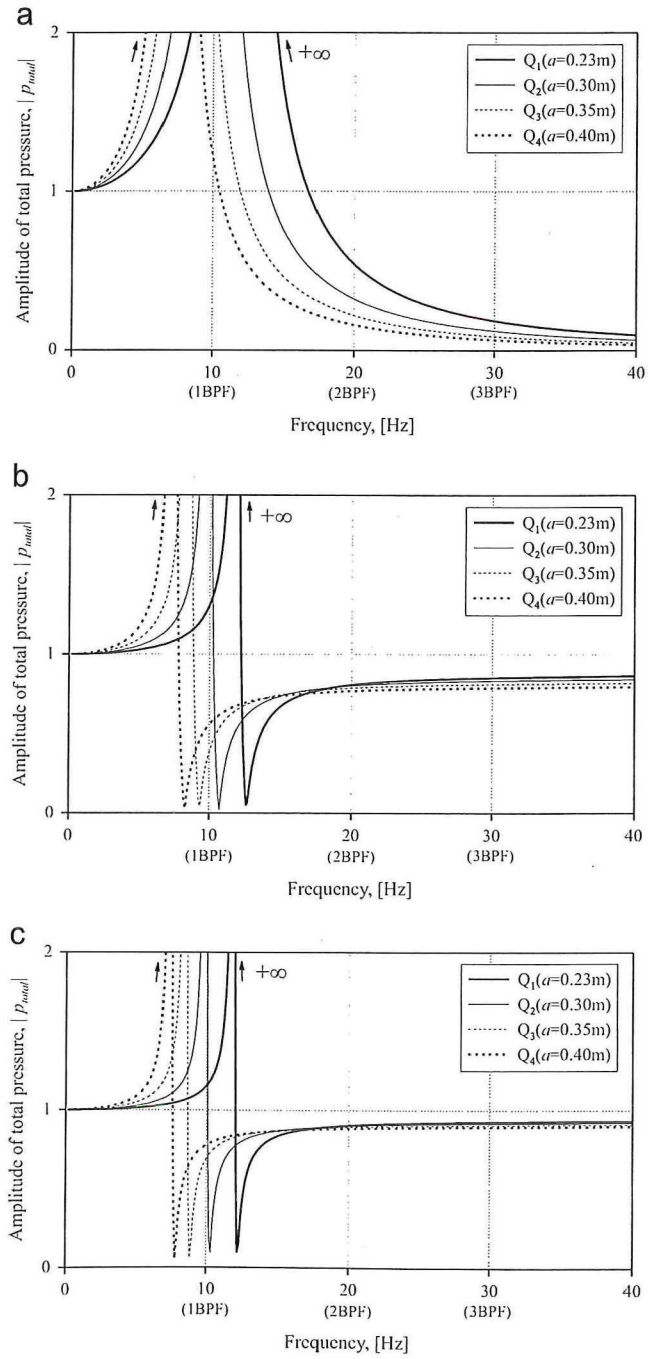

Fig. 12. Calculation of $|p_{total}|$ for comparison with experimental measurements: (a) $r=a$, at bubble boundary; (b) $r=2$ m, outside bubble; (c) $r=4$ m, outside bubble.

enhancement at the resonance frequency $k_w a|_{res}$

$$k_w a|_{res} = \sqrt{3gh^2} \tag{12}$$

This clearly shows that the resonance frequency of a bubble is inversely proportional to its size. Appendix A shows that the resonance frequency derived in this study is exactly identical to Minnaert's (1933) solution. Just above the resonance frequency, the real part of p_{scat} rapidly converges to $-(p_0 a)/r$ from negative infinity, whereas the imaginary part stays around zero. In particular, $Im(p_{scat})$ crosses zero at the frequency given in Eq. (13)

$$k_w a|_{Im(p_{scat})=0} = \sqrt{\frac{3gh^2}{1-a/r}} \tag{13}$$

It then diverges to negative infinity at high frequencies, which was outside the scope of this work.

Above the resonance frequency, the complex value p_{scat} converges to a pure real value with a negative sign. In more detail, analogous to the reflected wave from a pressure release surface, the scattered pressure p_{scat} above the resonance is in almost the opposite phase of the incident pressure p_{inc}. Thus, the total pressure p_{total} $(=p_{scat}+p_{inc})$ at those frequencies is smaller than the incident pressure p_{inc}, which yields destructive interference. Definitively, the total pressure is minimized at the zero crossing frequency of $Im(p_{scat})$, where p_{scat} becomes a pure negative real number.

Fig. 11 plots the amplitudes of the total pressure $|p_{total}|$ with the same parameters used to calculate p_{scat} in Fig. 9. Amplifications of the pressure amplitude, i.e., $|p_{total}| > p_0 = 1$, are first noted around the resonance frequency $k_w a|_{res}$. Even though the frequency responses above the resonance differ according to the observation point r, they demonstrate a clear reduction in pressure amplitude due to the destructive interference. Eq. (13) clarifies that the frequency of the maximum destructive interference approaches the resonance frequency with increasing r but is placed at an infinitely high frequency when $r=a$. Hence, the response on the bubble boundary shows a gradual reduction in pressure amplitude with increasing frequency and eventually resembles the characteristics of a simple isolator. On the other hand, when the observation point is apart from the bubble $(r>a)$ and the under-peak frequency moves to a lower range, the amount of reduction beyond the notch decreases with increasing frequency and distance. In short, the pressure reduction outside the bubble is mainly effective at low frequencies above the resonance.

Based on the previous analysis, an air bubble above the resonance frequency can reduce the pressure both on and outside its boundary. In the next subsection, we explain this in further detail through a comparison with experimental results.

3.2. Qualitative comparison with experimental data (effect of bubble size)

For comparison purposes, the radius of the equivalent bubble a needs to be determined beforehand. The cross-sectional area of the bubble sphere was simply assumed to be equal to that of the air layer at the propeller plane, as given in Table 2. Table 3 summarizes the estimated radius and corresponding resonance frequency. The bubble radius was varied from 0.23 m to 0.40 m to reflect the increase in airflow rate. Furthermore, the response on the bubble boundary was chosen as representative of P1. P2 and P3 were assumed to be 2 m and 4 m apart, respectively, from the origin of the bubble. Table 3 also includes the frequency of the maximum destructive interference along the observation point. The amplitude of the incident pressure p_0 was assumed to be unity; the total pressure $|p_{total}|$ shown in Fig. 12 was evaluated by Eq. (11). For convenient comparison with the measurements in Fig. 7, the readings at the first three BPFs are also prepared in Fig. 13.

Regarding to the first-order components, pressure amplitudes higher than unity at every location can now be determined by the resonant behavior of the bubble. As stated in the previous section, increasing the air injection from Q_1 to Q_4 shifted the resonance frequency of the equivalent bubble to lower values. In our case, the resonance frequency decreased from 12.8 Hz to 7.4 Hz, as shown in Table 3. Irrespective of the observation point, all of the first-order responses during the shifting $(Q_1 \rightarrow Q_2)$ increased until the resonance frequency of the bubble met the excitation frequency. For Q_3 and Q_4, i.e., when the bubble size was large enough that the corresponding resonance frequency was lower than the first BPF, the responses decreased again but in a different manner depending on the distance from the bubble. As shown in Table 3, the resonance frequency was still around the excitation frequency even for Q_3 or Q_4, and the frequency of the maximum destructive interference when $r>a$ was very close to the resonance frequency. As a result, the first-order responses on the bubble boundary belonged to the amplification zone, whereas the ones outside the bubble were around the zone of maximum destructive interference. This supports the considerable reduction in the first-order

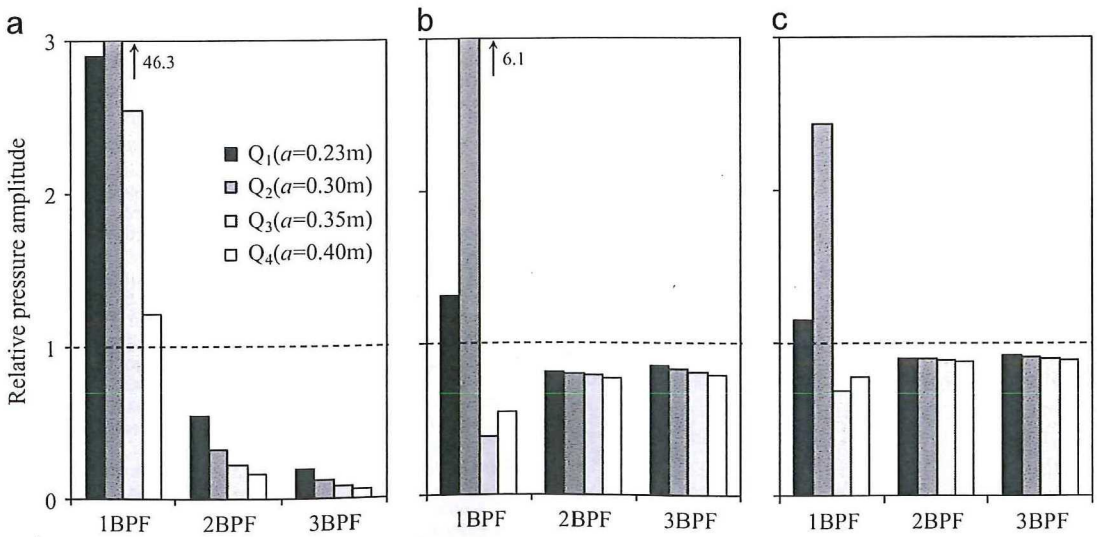

Fig. 13. Readings at first three BPFs for calculation shown in Fig. 12: (a) $r=a$, at bubble boundary; (b) $r=2$ m, outside bubble; (c) $r=4$ m, outside bubble.

hull excitation pressure outside the air-bubble layer. For reference, exaggerated predictions for the first-order components can be moderated by including damping in the theoretical model; however, this was outside the scope of this study.

The simple model described the measured qualitative behavior at high-order amplitudes well. On the bubble boundary, increasing the injection level (or bubble size) apparently produced a gradual increase in the air-cushioning effect at high frequencies. However, this was not the case outside the boundary. In other words, the pressure reduction with increased injection level became less significant as the distance from the bubble increased. Hence we can also be familiar with the high order components in Fig. 7.

4. Concluding remarks

In this study, our proposed single-nozzle air-injection scheme reduced the propeller cavitation-induced hull excitation pressure outside the air bubbles to a significant degree. This could not be attributed to an isolation mechanism. In order to qualitatively describe the observed behavior, we derived a simple theoretical model of acoustic scattering from a bubble through an approximation of Anderson's (1950) solution.

Although the proposed model does not account for every detail of the measured quantities, it provides crucial proof that the phase reversal reflection from the air bubble provoked a destructive interference effect, which can be considered as the key reason for the reduced pressure amplitude. In conclusion, a more efficient design for air injection that exploits the acoustic properties of air should be possible. Future research will involve the development of a more complicated bubble model that can yield a closer correlation with the measured values. In addition, the void fraction and bubble size distribution need to be measured to support the validity of the equivalent bubble assumption. We are currently conducting air-injection tests with the same compressor used in the full-scale trial at our water tunnel facility.

Acknowledgments

We are grateful to Mr. Orlando Faundez and Mr. Ramon Gatica at CSAV Southern Ship Management Chile and Mr. Maiken Empacher at A.P. Moller–Maersk Line for providing permission to perform tests on a full-scale ship. We also thank Captain Tadeusz Trzopek for providing a warm welcome and accommodating us when we were aboard. Finally, we thank Professor Yang-Hann Kim at Korea Advance Institute of Science and Technology for the insightful discussions.

Appendix A

The speed of sound for air bubble c_b is given as follows (Leighton, 1994)

$$c_b = \sqrt{\frac{B}{\rho_b}} \tag{A.1}$$

B denotes the bulk modulus of the air bubble under an adiabatic assumption and represents the pressure change dP from the equilibrium state of P_0 and V_0 in response to the volume change dV

$$B = -V_0 \frac{dP}{dV} \tag{A.2}$$

Further, the adiabatic gas process yields

$$P_0 V_0^{\gamma} = constant, \tag{A.3}$$

where γ (=1.4 for air) is the specific heat ratio. Applying the chain rule to the above results in the following:

$$\frac{dP}{dV} = -\frac{P_0 \gamma}{V_0} \tag{A.4}$$

By substituting Eqs. (A.2) and (A.4) into Eq. (A.1) and further substituting into Eq. (12), we can then rewrite the resonance frequency of the bubble sphere $f|_{res}$ as

$$f|_{res} = \frac{1}{2\pi a}\sqrt{\frac{3P_0\gamma}{\rho_w}}, \tag{A.5}$$

which is exactly identical to Minnaert's (1933) resonance frequency.

References

Anderson, V.C., 1950. Sound scattering from a fluid sphere. J. Acoust. Soc. Am. 22, 426–431, http://dx.doi.org/10.1121/1.1906621.
Bendat, J.S., Piersol, A.C., 2010. Random Data: Analysis and Measurement Procedures, fourth ed. John Wiley & Sons.
Brennen, C.E., 1995. Cavitation and Bubble Dynamics. Oxford University Press, New York.
Carlton, J., 2007. Marine Propellers and Propulsion, second ed. Butterworth-Heinemann, USA.
Carstensen, E.L., Foldy, L.L., 1947. Propagation of sound through a liquid containing bubbles. J. Acoust. Soc. Am. 19, 481–501, http://dx.doi.org/10.1121/1.1916508.
Cumming, R.A., Morgan, W.B., Boswell, R.J., 1972. Highly skewed propellers. Soc. Naval Archit. Mar. Eng. Trans. 80, 98–135.
Friesch, J., 1992. Possibilities of Model Tests for Energy Saving Devices. Hydrodynamics: Computations, Model-tests and Reality. Elsevier Science Publishers B.V. (H.J.J van den Boom. (Ed.).
Johansen, J.P., Castro, A.M., Carrica, P.M., 2010. Full-scale two-phase flow measurements on Athena research vessel. Int. J. Multiphase Flow 36 (9), 720–737, http://dx.doi.org/10.1016/j.ijmultiphaseflow.2010.05.002.
Kim, Y.H., 2010. Sound Propagation: An impedance Based Approach. John Wiley & Sons.
Kinns, R., Bloor, C.D., 2004. Hull vibration excitation due to monopole and dipole propeller sources. J. Sound Vib. 270, 951–980, http://dx.doi.org/10.1016/S0022-460X(03)00641-2.
Krüger, S., Friesch, J., Stoye T., 2004. Reduction of propeller induced pressure fluctuation by systematic air injection. In: Ninth Symposium on Practical Design of Ships and Other Floating Structures. Lüebeck-Travemüende, Germany.
Lee, J.H., Kim, K.J., 2007. Modeling of nonlinear complex stiffness of dual-chamber pneumatic spring for precision vibration isolations. J. Sound Vib. 301, 909–926, http://dx.doi.org/10.1016/j.jsv.2006.10.029.
Lee, J.H., Kim, K.J., 2009. A method of transmissibility design for dual-chamber pneumatic vibration isolator. J. Sound Vib. 323, 67–92, http://dx.doi.org/10.1016/j.jsv.2008.12.028.
Leighton, T.G., 1994. The Acoustic Bubble. Academic Press, London.
Lindgren, H., Johnsson, C.A., 1980. On the Influence of Cavitation on Propeller Excited Vibratory Forces and Some Means of Reducing its Effect. Publications of Swedish Maritime Research Centre, Göteborg, Sweden, No. 84.
Minnaert, M., 1933. On musical air-bubbles and sounds of running water. Philos. Mag. 104, 235–248.
Morse, P.M., Ingard, K.U., 1987. Theoretical Acoustics. Princeton University Press, Princeton.
Nicholas, M., Roy, R.A., Crum, L.A., Oğuz, H., Prosperetti, A., 1994. Sound emissions by a laboratory bubble cloud. J. Acoust. Soc. Am. 95, 3171–3182, http://dx.doi.org/10.1121/1.409981.
Nilsson, A.C., 1980. Propeller induced hull plate vibrations. J. Sound Vib. 69, 539–557, http://dx.doi.org/10.1016/0022-460X(80)90624-0.
Ødegaard, J., 2006. Practical experience with reduction of propeller-induced noise and vibration. In: Proceedings of the Second International Ship Noise and Vibration Conference. London, UK.
Ross, D., 1976. Mechanics of Underwater Noise. Pergamon Press, New York.
Terril, E.J., Fu, T., 2008. At-sea measurements for ship hydromechanics. In: 27th Symposium on Naval Hydrodynamics. Seoul, Korea.
Ukon, Y., Fujisawa, J., Kudo, T., 2000. Reduction of pressure fluctuations induced by cavitating propellers due to air injection through the hull at the stern of a ship. Trans. West Jpn. Soc. Naval Archit. 99, 33–42.
Weitendorf, E.A., 1981. Cavitation phenomena, propeller excited hull pressure amplitudes and cavitation scale effect. Ocean Eng. 8 (5), 517–539, http://dx.doi.org/10.1016/0029-8018(81)9001.7-2.
Wijngaarden, E., Brouwer, J., Zijlstra, M., 2006. A spatial extrapolation technique for sparse measurements of propeller-induced hull-pressures using an inverse acoustic boundary element method. In: Sixth International Symposium on Cavitation. CAV, 2006, Wageningen, Netherlands.
Wikipedia, (2013). ⟨http://en.wikipedia.org/wiki/Beaufort_scale⟩. (accessed 1 March).